Solid State Ionics 444 (2026) 117268

Contents lists available at ScienceDirect

Solid State Ionics

journal homepage: www.elsevier.com/locate/ssi

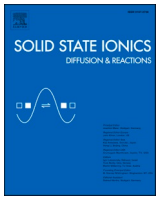

A Li-ion battery electrolyte realized by encapsulation of a Li-containing ionic liquid in the metal-organic framework ZIF-8

Wen Yang [a,b], Christian Rodenbücher [a], Jiangshui Luo [c,*], Carsten Korte [a,*]

[a] Institute of Energy Technologies (IET-4), Forschungszentrum Jülich GmbH, Jülich, Germany
[b] Faculty of Mathematics, Computer Science and Natural Sciences, RWTH Aachen University, Aachen, Germany
[c] College of Materials Science and Engineering, Sichuan University, Chengdu, China

ARTICLE INFO

Keywords:
MOF
Ionic liquids
Cage expansion
Swing effect electrolyte
Battery

ABSTRACT

Metal–organic frameworks (MOFs) are promising host materials for studying and controlling the dynamics of molecules and ions, including lithium ions. In this study, a lithium-ion-containing ionic liquid (IL) was successfully incorporated into the MOF ZIF-8, and its phase behavior and ionic conductivity were investigated. Using a capillary action method, lithium bis(trifluoromethanesulfonyl)imide (Li[TFSI])-containing 1-ethyl-3-methylimidazolium bis(trifluoromethylsulfonyl)imide ([Emim][TFSI]), denoted as $Li_{0.2}[Emim]_{0.8}[TFSI]$, was introduced into the pores of ZIF-8. The impact of varying $Li_{0.2}[Emim]_{0.8}[TFSI]$ concentrations on the crystal structure, bond vibrations, and ionic conductivity was systematically analysed. Structural analysis revealed an increase in the lattice constant of ZIF-8 upon $Li_{0.2}[Emim]_{0.8}[TFSI]$ encapsulation, accompanied by a weakening of the N–Zn–N bond as the cage structure expanded. Additionally, the migration of Li[TFSI] ion pairs into the cages disrupts ion pair interactions, leading to a reduction in the O=S=O bond strength within the $[TFSI]^-$ anion. When the ZIF-8 pores were fully saturated with $Li_{0.2}[Emim]_{0.8}[TFSI]$, the composite exhibited an ionic conductivity of 0.36(2) $mS{\cdot}cm^{-1}$ at 80 °C, with the activation energy of 0.26(1) eV. Its ionic conductivity meets the performance criteria required for use in lithium-ion battery electrolytes. However, it has the low lithium transference number. And the $LiCoO_2$||Li coin cells with $LEI_{1.2}$@ZIF pellet has a capacity retention of 74.9% only after 100 cycles at 0.2C at room temperature. Compared with the pure lithium-salt-containing ionic liquid, $Li_{0.2}[Emim]_{0.8}[TFSI]$, the quasi-solid-state electrolyte $LEI_{1.2}$@ZIF, prepared by incorporating the lithium-salt-containing ionic liquid into the ZIF-8 framework, exhibits inferior electrochemical performance in lithium batteries. This is primarily due to the ionic conductivity that is two orders of magnitude lower and a higher interfacial impedance of the quasi-solid-state electrolyte $LEI_{1.2}$@ZIF. These findings highlight the potential of MOF-based composites as quasi-solid-state or solid-state electrolytes for lithium-ion battery applications.

1. Introduction

Lithium solid-state batteries are considered promising candidates for next-generation energy storage systems due to their ability to mitigate the risks of volatilization, leakage, and fire associated with conventional liquid Li-ion batteries [1,2]. Currently, solid-state electrolytes are primarily classified into polymer-based and inorganic ceramic-based electrolytes. However, polymer electrolytes suffer from relatively low ionic conductivity and instability under high voltages [3,4]. Common polymer electrolytes include polyethylene oxide (PEO), poly(vinylidene fluoride) (PVDF), poly(vinylidene fluoride-*co*-hexafluoropropylene) (PVDF-HFP), and polypropylene carbonate (PPC) [5]. On the other hand, inorganic ceramic electrolytes, such as oxide-based systems (e.g., perovskites and garnets) and sulfide-based materials (e.g., thio-LISICONs and halide-containing compounds like Li_6PS_5X and Li_4PS_4X, where X is a halogen), face challenges such as poor chemical and electrochemical stability, as well as inadequate interfacial contact with electrodes [6,7]. These limitations highlight the urgent need to explore alternative solid-state electrolytes with improved performance.

A novel class of solid-state electrolytes, denoted as Li-IL@MOFs, consists of a lithium-conductive salt dissolved in an IL and encapsulated within a metal–organic framework (MOF) [8,9]. MOFs are a family of crystalline nanoporous materials composed of metal ions and organic ligands, offering a highly tunable and stable three-dimensional (3D)

* Corresponding authors.
E-mail addresses: jiangshui.luo@scu.edu.cn (J. Luo), c.korte@fz-juelich.de (C. Korte).

https://doi.org/10.1016/j.ssi.2026.117268
Received 4 May 2026; Received in revised form 30 June 2026; Accepted 3 July 2026
Available online 8 July 2026
0167-2738/© 2026 The Authors. Published by Elsevier B.V. This is an open access article under the CC BY license (http://creativecommons.org/licenses/by/4.0/).

framework. In this design, the porous MOF serves as a host material, while the confined Li salt/IL functions as a Li^+ conductor [10]. These materials have some intrinsic advantages. The tunable pore sizes of MOFs can effectively confine anions, thereby promoting the dissociation of lithium salts and facilitating the free movement of Li^+ ions. These properties promote Li^+ transfer, thereby increasing the Li^+ transference number [11–13]. The periodic crystalline structure and ordered channels of MOFs enable a uniform Li^+ flux, which facilitates homogeneous Li^+ electrodeposition during charge–discharge cycles, effectively restricting lithium dendrite growth. Sun et al. successfully encapsulated Li[TFSI]-containing [Emim][TFSI] (Emim: 7.6 Å, TFSI: 7.9 Å) within UiO-66 MOF [$Zr_6O_4(OH)_4(BDC)_4$, BDC = 1,4-benzenedicarboxylate ($C_6H_4(CO_2)_2$)]. Wu et al. successfully encapsulated Li[TFSI]-containing [Deme][TFSI] (N,N-Diethyl-*N*-methyl-N-(2-methoxyethyl)ammonium bis(trifluoromethanesulfonyl)imide) and [Emim][TFSI] within the stable UiO-66-NH_2 MOF, demonstrating that MOFs can effectively serve as host materials for Li-ion conduction in battery applications [9]. Sun et al. successfully encapsulated Li[TFSI]-containing [Emim][TFSI] (Emim: 7.6 Å, TFSI: 7.9 Å) within UIO-66 [14]. The $[Emim]^+$ and $[TFSI]^-$ ions were immobilized by the ordered skeleton structure and interconnected channels of UIO-66, leading to a high Li^+ transference number and uniform Li plating in lithium metal batteries. Pan et al. introduced [$Emim_{0.8}Li_{0.2}$][TFSI] into the pores of MOF-525(Cu), demonstrating excellent compatibility with both the active $LiFePO_4$ cathode and the Li metal anode. The composite electrolyte exhibited low interfacial resistance at the cathode and facilitated uniform Li deposition at the anode, attributed to its superior mechanical stability [15].

There are a number of research on the ZIF-8 MOF. ZIF-8, a zinc-based three-dimensional metal–organic framework, was chosen as the model MOF. ZIF-8 is a 2-methylimidazole zinc salt, i.e. $Zn^{2+}(CH_3C_4H_2N_2^-)_2$. It has a cubic ($I\bar{4}3m$) zeolite-type structure with 2 sodalite cages per unit cell and a lattice constant $a = 16.9956(12)$ Å [16]. ZIF-8 presents several advantages that make it a promising candidate for use in lithium battery electrolytes. It exhibits excellent thermal and chemical stability, well-defined crystallinity. Its high surface area and porous framework facilitate efficient Li^+ ion transport. Fujie et al. introduced a mixture of Emi-TFSA (1-ethyl-3-methylimidazolium bis(trifluoromethylsulfonyl)amide) with LiTFSA (lithium bis(trifluoromethylsulfonyl)amide) inside ZIF-8 pores, and found The $TFSA^-$ anions showed a gradual decrease of mobility in the micropores at low temperatures, which indicates the absence of the apparent freezing transition [17]. Hessling et al. investigates how interactions between different ionic liquid-based electrolytes and ZIF-8 influence the coordination and dynamics of Li^+ in confinement [18]. The result shows the beneficial interactions in the confined system can even make Li^+ the fastest diffusing species, in contrast to bulk electrolyte, where Li^+ transport is limited by strong Li-anion clusters.

The introduction of guest molecules into the cage may generate an internal stimulus that induces structural expansion of ZIF-8, allowing its apertures to adapt and accommodate guest molecules. This dynamic behavior expands the potential applications of ZIF-8 for molecular encapsulation. Numerous studies have demonstrated the successful encapsulation of various molecules within ZIF-8 cages. Zheng et al. successfully encapsulated Rhodamine 6G (R6G), with a molecular diameter of 11.3–13.7 Å, inside ZIF-8 pores [19]. He et al. encapsulated [Bmim][TFSI] inside the ZIF-8 [20]. Although these guest molecules have diameters larger than the nominal ZIF-8 aperture size (3.4 Å), their successful encapsulation is attributed to the intrinsic flexibility of the ZIF-8 framework, which allows temporary pore expansion to accommodate larger molecules. Tang employed molecular dynamics (MD) simulations to investigate the effect of a water/methanol mixture on the structural flexibility of ZIF-8 [21]. The study found that the water/methanol mixture slightly influences the flexibility of the ZIF-8 framework, as characterized by variations in the swing dihedral angle and aperture diameter. Hu et al. utilized density functional theory and MD simulations to analyse the variation in ZIF-8 aperture configurations when filled with different amounts of CO_2/CH_4 [22]. The study identified five distinct aperture structures, each with a different window diameter. The pristine ZIF-8 aperture has a diameter of 3.4 Å, which expands to 4.1 Å, 4.2 Å, 4.7 Å, and 6.9 Å as more CO_2/CH_4 molecules are encapsulated within the cages. This expansion of ZIF-8 pores is primarily attributed to the rotation of the organic ligand, 2-methylimidazole, and a phenomenon known as the "swing effect". This effect allows the ZIF-8 framework to adjust its aperture size in response to guest molecule adsorption. Previous work demonstrated, that the $I\bar{4}3m$ space-group of ZIF-8 is maintained in a high-pressure phase. As pressure increases, additional solvent can be compelled into the nanopores, despite a reduction in the nanopore volume. Eventually, the sample undergoes a reorientation of the imidazolate linkers. This transition does not only facilitate the entry of more solvent into the original nanopores, but also enlarges the narrow channels connecting these pores. Consequently, there is an overall augmentation in porous volume and an increase in the size of the 6-ring windows [23].

These findings promote the potential of MOF-based electrolytes in enhancing ionic conductivity and advancing solid-state battery technology. However, understanding the interaction between Li-ILs and MOF frameworks is crucial for their large-scale application in lithium metal batteries. This requires deeper insight into how the MOF structure changes when Li-ILs enter the cages, and how these cages immobilize the Li-ILs within their confines. However, knowing the interaction between Li-ILs and MOF frameworks is crucial for their application in lithium metal batteries. This requires a deeper understanding of how the structure change when Li-ILs going inside the MOF cages, and how the cages immobilized the Li-IL inside the cages.

In this work, We encapsulate Li[TFSI]-containing [Emim][TFSI] within ZIF-8 (Basolite®) to fabricate a solid-state Li-ion electrolyte. Li[TFSI]-containing [Emim][TFSI] offers significant advantages over conventional carbonate-based electrolytes for lithium metal batteries, including non-flammability and high thermal stability. Moreover, its non-volatile and highly ionic nature makes it particularly well suited for confinement within MOF structures. We systematically investigate the interaction between the lithium salt-containing IL and the ZIF-8 framework, focusing on its structural changes, ion pair interactions, total ionic conductivity, and activation energy. These findings provide valuable insights into the potential application of MOF-based electrolytes in Li-ion batteries, offering a foundation for further advancements in this field.

2. Experimental

LiTFSI (Lithium bis(trifluoromethylsulfonyl)amide) (purity: 99.99%), [Emim][TFSI] (1-Ethyl-3-methylimidazolium bis(trifluormethylsulfonyl)imide) (purity ≥99%, $H_2O \leq 500$ ppm) and ZIF-8 (Zn (2-imidazole)$_2$) were purchased from Sigma-Aldrich (USA) company and used without further purification. $Li_{0.2}[Emim]_{0.8}[TFSI]$ was prepared by mixture of Li[TFSI] and [Emim][TFSI].

The synthesis of [Emim][TFSI]@ZIF-8 was carried out through the capillary action. In this process, [Emim][TFSI] and ZIF-8 were first manually mixed using a mortar and pestle, then transferred to a vacuum oven and heated at 105 °C overnight to ensure uniform distribution. 100 mg ZIF-8 powder was mixed with 13.26 μL, 26.52 μL, 39.78 μL, 53.04 μL, 66.30 μL and 79.56 μL [Emim][TFSI], respectively. The quantity ratios of [Emim][TFSI] molecules to ZIF-8 cages were as follows: 1.39:1, 2.78:1, 4.16:1, 5.55:1, 6.94:1, and 8.34:1, these ratios were determined to correspond to the theoretical pore volume of ZIF-8 at loadings of 20%, 40%, 60%, 80%, 100% and 120%, respectively. The volume occupancy was derived from the pore volume of ZIF-8 (0.663 cm^3/g), as determined through BET analysis, and the density of [Emim][TFSI] (1.5214 g/cm^3 at 20 °C), as shown in literature [24]. In a typical synthesis procedure, 66.30 μL of [Emim][TFSI] and 100 mg of dehydrated ZIF-8 were mixed

using a mortar and pestle. Subsequently, the resulting powders were subjected to overnight drying under vacuum conditions at 105 °C. This particular sample was denoted as $EI_{1.0}$@Z, which signifies the combination of 66.3 μL [Emim][TFSI] with 100 mg ZIF-8. A similar procedure was applied to prepare samples designated as EI_x@Z, where x values corresponded to 0.2, 0.4, 0.6, 0.8, 1, and 1.2.

As shown in Fig. 1(a), $Li_{0.2}[Emim]_{0.8}[TFSI]$ was prepared by mixing Li[TFSI] and [Emim][TFSI] while stirring until a clear, homogeneous solution is obtained in a glove box under argon. A total of 100 mg of ZIF-8 powder was combined with 13.26 μL, 26.52 μL, 39.78 μL, 53.04 μL, 66.30 μL, and 79.56 μL of $Li_{0.2}[Emim]_{0.8}[TFSI]$, respectively. The mixtures were ground using a mortar and pestle at molar ratios of 0.39:1.16:1, 0.79:2.32:1, 1.19:3.49:1, 1.58:4.65:1, 1.98:5.81:1, and 2.38:6.97:1 (Li[TFSI]:[Emim][TFSI]:ZIF-8). These ratios correspond to theoretical micropore volume occupancies of 20%, 40%, 60%, 80%, 100%, and 120%, respectively. The resulting composites were designated as $LEI_{0.2}$@ZIF, $LEI_{0.4}$@ZIF, $LEI_{0.6}$@ZIF, $LEI_{0.8}$@ZIF, LEI_1@ZIF, and $LEI_{1.2}$@ZIF. That is to say, there are averaged 1.98 Li^+, 5.81 $[Emim]^+$ and 7.79 $[TFSI]^-$ in one ZIF-8 cage for LEI_1@ZIF, which fully occupied the pores volume in ZIF-8. The volumetric occupancies were calculated from the pore volume of ZIF-8 (0.663 cm^3/g), density of $Li_{0.2}[Emim]_{0.8}[TFSI]$ (1.571 g/cm^3 at 20 °C). The mixtures were heated and stored overnight to enhance the diffusion of $Li_{0.2}[Emim]_{0.8}[TFSI]$ inside the pores of ZIF-8. All preparation process were carried out in a glovebox to prevent water absorption of the mixture.

The nitrogen adsorption and desorption isotherms (Brunauer, Emmett and Teller, BET) were measured at 77 K (Micromeritics Gemini VII, USA). Powder X-ray diffraction (PXRD) of the samples were performed by using a Bruker D8 Advanced diffractometer (Germany), employing Cu-K_α radiation (λ = 1.5418 Å). The diffractograms were evaluated by Rietveld refinement, employing the Profex software [25]. Infrared spectroscopy (IR) analyses were conducted using a Nicolet spectrometer with GladiATR™ ATR unit (USA), spanning the wavenumber range of 400 to 4000 cm^{-1}.

The electrochemical measurements of [Emim][TFSI] and $Li_{0.2}[Emim]_{0.8}[TFSI]$ liquids were performed using a two-electrode configuration inside a Faraday cage (VistaShield™ , Gamry Instruments, USA) with a potentiostat (Zennium, ZAHNER Elektrik GmbH, Germany). The cell consisted of a cylindrical platinum vessel, which also functioned as the counter electrode. A high-purity platinum wire (99.95%, Goodfellow GmbH, Germany) positioned at the center of the vessel served as the working electrode. EIS measurement was applied within the temperature range between 20 °C and 80 °C with a step of 10 °C. The electrochemical measurement procedure of EI@ZIF-8 and LEI@ZIF-8 powders is shown in Fig. 1(b). Initially, the powders were compressed into pellets using cold pressing at 2 MPa. Each pellet had a diameter of 6.3 mm and a thickness of 3.0 mm. A four-probe method was employed for EIS to eliminate contact resistance between the electrode and electrolyte. Platinum electrodes with a diameter of 1 mm were used. EIS measurements were conducted over a temperature range of 20 °C to 80 °C in 10 °C increments. Each test was repeated three times at 5-h intervals to ensure reliability. The overall conductivity (σ/S) of the sample was determined using Eq. 1 [26].

$$\sigma = \frac{1}{2\pi r R} \tag{1}$$

where σ is the overall conductivity, r is the distance of the two inner probes and R is the measured resistance from impedance spectroscopy. It is worth noting that the ionic conductivity of all the samples exhibited an Arrhenius behavior, characterized by an increase in conductivity with rising temperature. The activation energy E_a for ion transport, expressed in eV, was computed by fitting the conductivity data according to the Arrhenius equation (Eq. 2):

$$\sigma T = \sigma_0 \, e^{-\frac{E_a}{k_B T}} \tag{2}$$

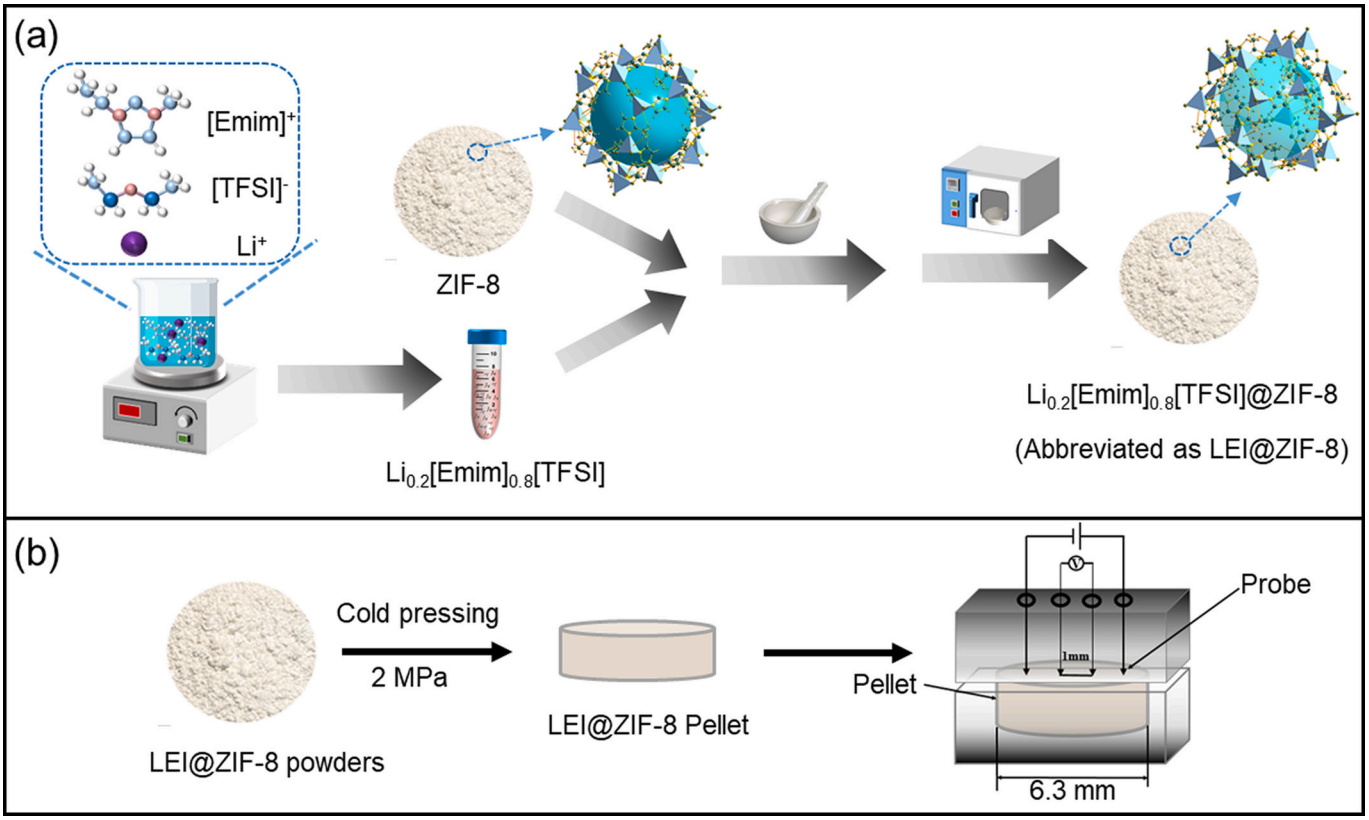

Fig. 1. Flow chart of (a) synthesis process and (b) electrochemical impedance spectroscopy (EIS) of $Li_{0.2}[Emim]_{0.8}[TFSI]$@ZIF-8 composites.

where k_B is the Boltzmann constant and T is the temperature. The lithium-ion transference number (t_{Li}^{+}) was determined by using a combined electrochemical technique involving direct current (DC) polarization and alternating current (AC) impedance spectroscopy in a symmetric Li||Li coin cell configuration. The value of $t_{Li}{}^{+}$ was calculated according to the following equation:

$$t_{Li^+} = \frac{I_s(\Delta V - I_0 R_1^0)}{I_0(\Delta V - I_s R_1^s)} \quad (3)$$

where ΔV is the applied DC potential (10 mV); I_0 and I_s represent the initial and steady-state currents, respectively, during the DC polarization process; and R_1^0 and R_1^s denote the interfacial resistances of the symmetric Li||Li cell before and after DC polarization, respectively. The electrochemical stability window of the electrolyte was evaluated using linear sweep voltammetry (LS*V*). A lithium metal foil was employed as working electrode, while a stainless-steel sheet served as the counter (and reference) electrode. The potential was scanned from 2 to 6 V at a scan rate of 1 mV s^{-1}.

$LiCoO_2$, Super P carbon, and PVDF were dispersed in 1-methyl-2-pyrrolidinone (NMP) and homogenized by ball milling for 1 h at room temperature. The resulting slurry was then cast onto an aluminum foil current collector and dried in a vacuum oven at 80 °C overnight. The weight ratio of $LiCoO_2$: Super P: P*V*DF was 7:1:2. After drying, the electrodes were punched into circular disks with a diameter of 12 mm. 2032-type coin cells were assembled in an argon-filled glovebox, using the $LiCoO_2$ composite cathodes, $LEI_{1.2}$@ZIF electrolyte membranes, and lithium metal anodes. The assembled $LiCoO_2$||Li cells were galvanostatically cycled between 3.0 and 4.15 V (vs. Li/Li^+) at various current densities of 0.2, 0.4, 0.6, 1.0, and 2.0C (1C = 138 mA g^{-1}) using a Neware CT-4008Q battery testing system. The cycling performance was measure at 0.2C for all the membrane with differrent volume ratio of ZIF-8.

3. Results and discussion

To assess the pore characteristics of the $Li_{0.2}[Emim]_{0.8}[TFSI]$@ZIF-8 composites, nitrogen (N_2) adsorption and desorption experiments were performed at 77 K, as shown in Fig. 2(a). Both pristine ZIF-8 and $Li_{0.2}[Emim]_{0.8}[TFSI]$@ZIF-8 exhibited type I isotherms, characterized by a sharp initial rise in adsorption at low relative pressures, followed by a plateau at higher pressures. This adsorption behavior is indicative of the presence of micropores within the material. As presented in Fig. 2 (b), the BET surface area and pore volume of pristine ZIF-8 were determined to be 1452(22) m^2/g and 6423(89) × 10^{-4} cm^3/g, respectively. Upon encapsulation of $Li_{0.2}[Emim]_{0.8}[TFSI]$@ZIF-8, a gradual decline in both BET surface area and pore volume was observed, signifying the successful incorporation of the IL within the porous framework. At the maximum loading of $LEI_{1.0}$@Z, the BET surface area and pore volume decreased significantly to 0.97(5) m^2/g and 1.6(5) × 10^{-4} cm^3/g, respectively. This substantial reduction confirms the effective occupation of ZIF-8 pores by the IL. Interestingly, the measured pore volume no longer decreases significantly above $LEI_{0.6}$@ZIF-8, suggesting that a substantial fraction of the pore network becomes inaccessible to N_2 molecules during adsorption measurements. Similar behavior has been reported for ionic-liquid-loaded porous materials, where guest species located near pore apertures partially block pore entrances and restrict gas diffusion into the internal cavities [27]. Consequently, the apparent BET surface area and pore volume can decrease much more strongly than expected from pore filling alone, leading to an underestimation of the actual residual porosity of the host framework. In the present system, LiFSI-containing ionic liquid is likely distributed not only within the ZIF-8 cages but also near pore windows and on external crystal surfaces, thereby hindering N_2 access to the internal pore network during physisorption measurements.

As depicted in Fig. 3(a) and (b), Powder X-ray diffraction (PXRD) analysis unveiled the original ZIF-8 XRD peaks shifted to the lower angles gradually with the increase of $Li_{0.2}[Emim]_{0.8}[TFSI]$ amount inside the ZIF-8 cages. The refinement results are shown in Fig. S1 and S2. The lattice constant of $Li_{0.2}[Emim]_{0.8}[TFSI]$@ZIF-8 is exemplified in Fig. 3 (c). The results confirmed that pristine ZIF-8 exhibits a body centred cubic structure with the sodalite cages and the space group $I\bar{4}3m$, proving lattice parameters a = 17.0230(2) Å. $Li_{0.2}[Emim]_{0.8}[TFSI]$ @ZIF-8 samples also maintained a body centred cubic structure with the space group $I\bar{4}3m$, but with slightly enlarged lattice parameters. This observation implies that the fundamental crystal structure of ZIF-8 remains unaltered, but the encapsulation of $Li_{0.2}[Emim]_{0.8}[TFSI]$ induces a modest expansion of the ZIF-8 sodalite cages. Fig. 3 (c) shows that the change of lattice constant of ZIF-8 have a linear relationship with the amount of $Li_{0.2}[Emim]_{0.8}[TFSI]$ encapsulating inside the ZIF-8 cages.

The ZIF-8 framework features intrinsic porous cavities with a diameter of approximately 12 Å and a narrow aperture of around 3.4 Å (see Fig. 4), which plays a crucial role in guest molecule uptake [28]. Fig. 4 is a schematic illustration designed to provide a clear visualization for the reader. The number of Li-IL ion pairs within each cage was theoretically calculated using the BET pore volume and Li-IL density. In Fig. 4, the lattice constants for each sample were derived from the XRD and Rietveld refinement results. The sodalite cages exhibit structural flexibility, allowing expansion upon hosting $Li_{0.2}[Emim]_{0.8}[TFSI]$ molecules, as confirmed by XRD results. As shown in Fig. 4(a)-(f) and Fig. S

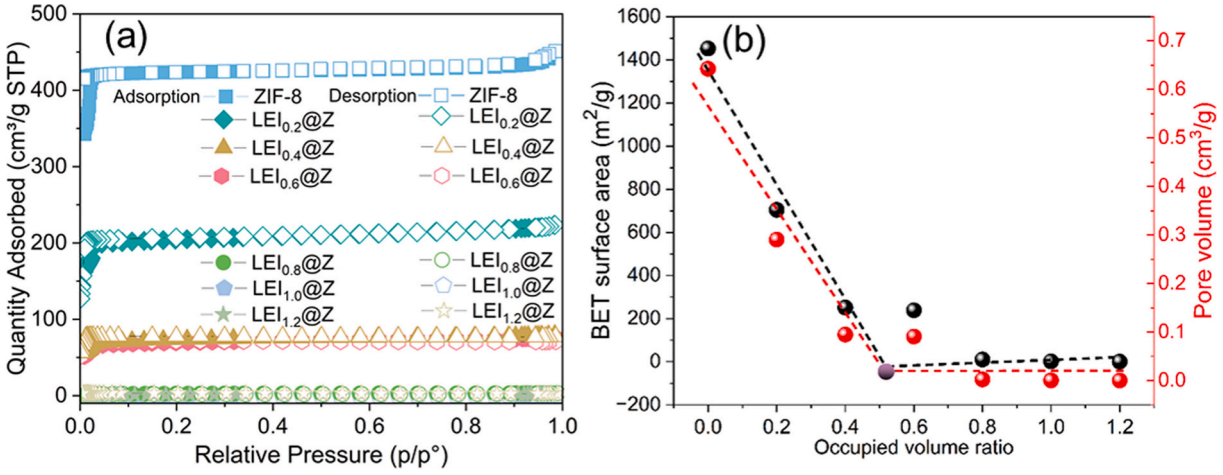

Fig. 2. (a) N_2 adsorption-desorption isotherms of $Li_{0.2}[Emim]_{0.8}[TFSI]$@ZIF-8 at 77 K. (b) Variation of BET specific surface area and pore volume of LEI@ZIF with percentage of occupied pore space in ZIF-8 cages. (STP: Standard temperature and presure).

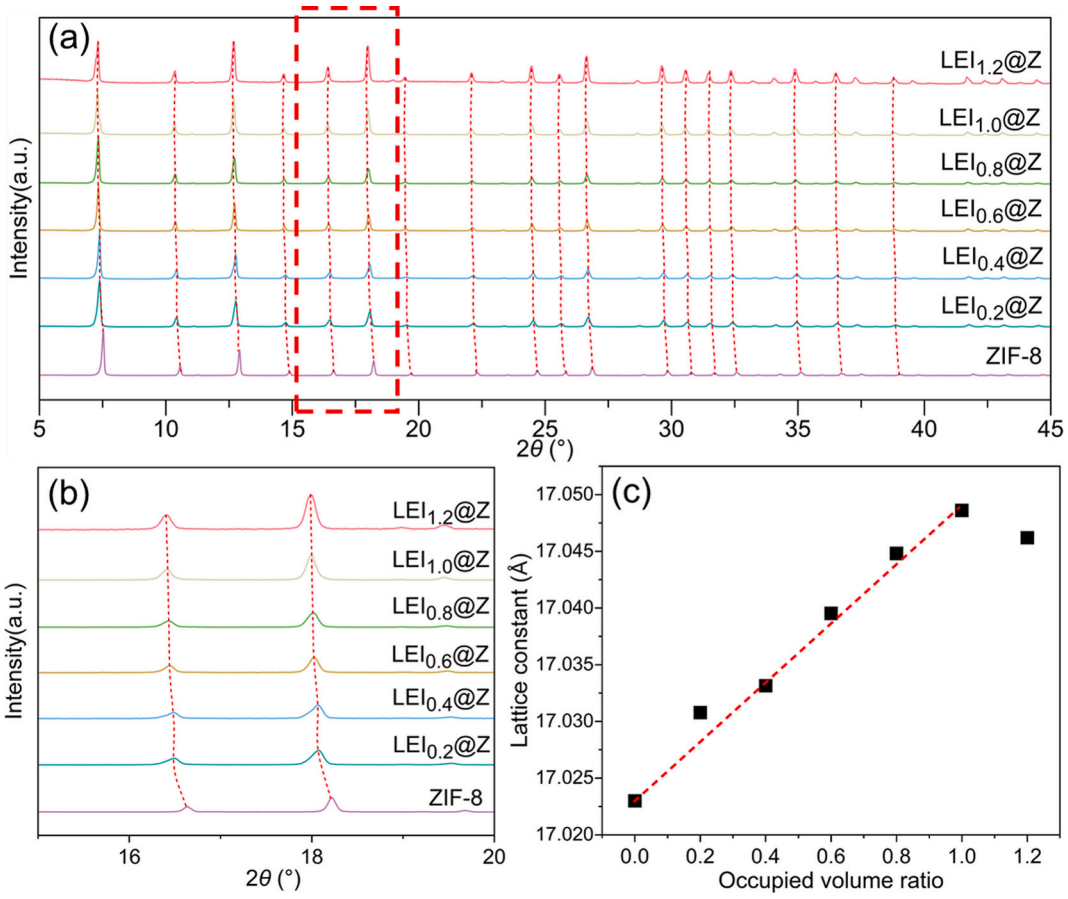

Fig. 3. (a) PXRD patterns of LEI@ZIF. (b) Magnification of Fig. 1(a) in the range between 15° and 20°. (c) The change of lattice constant of ZIF-8 cages in the function of occupied volume ratio by $Li_{0.2}[Emim]_{0.8}[TFSI]$.

(1)–(2), the original lattice constant of ZIF-8 is 17.0230(2) Å. When an average of 2.55 $Li_{0.2}[Emim]_{0.8}[TFSI]$ ion pairs are introduced into the pores, the lattice expands to 17.0308(3) Å (+0.047%). Further expansion is observed with increasing ion pair uptake: 3.11 ion pairs → 17.0331(4) Å (+0.059%), 4.58 ion pairs → 17.0395(4) Å (+0.094%), 6.23 ion pairs → 17.0448(5) Å (+0.129%). The maximum expansion occurs at 17.0491(5) Å (+0.153%) when 7.79 $Li_{0.2}[Emim]_{0.8}[TFSI]$ ion pairs fully occupy the pore volume. This behavior arises because $Li_{0.2}[Emim]_{0.8}[TFSI]$ ion pairs initially enter the ZIF-8 cages, generating internal pressure within the framework. Once the cages become fully occupied, additional ion pairs remain outside the pores, creating external pressure that counterbalances the internal stress induced by the confined species. As a result, the ZIF-8 cage size in $LEI_{1.2}$@ZIF-8 becomes smaller than $LEI_{1.0}$@ZIF-8, even though it contains a higher amount of $Li_{0.2}[Emim]_{0.8}[TFSI]$ than $LEI_{1.0}$@ZIF-8.

Our previous work introduced [Emim][TFSI] into the ZIF-8 cages and resulted in a maximum cage expansion of approximately 1.17% [27]. However, when a portion of [Emim][TFSI] was replaced with LiTFSI, the cage expansion decreased significantly to 0.153%. This behavior can be attributed to the strong coordination between Li^+ and $TFSI^-$ upon the addition of LiTFSI. The $[TFSI]^-$ anions become partially involved in the Li^+ solvation shell, leading to the formation of Li–TFSI complexes or aggregates. As a result, the confined electrolyte structure differs substantially from that of pure [Emim][TFSI]. The strong Li^+–$TFSI^-$ interactions promote a more compact and ordered ionic arrangement, reducing the extent to which the confined species exert outward stress on the ZIF-8 framework. In addition, the formation of $Li(TFSI)_x$ aggregates may reduce the mobility and accessibility of the electrolyte species within the ZIF-8 pore network compared with pure [Emim][TFSI]. Consequently, the effective loading of guest species inside the cages may decrease, which would further reduce the framework expansion. Therefore, despite the presence of Li–TFSI coordination complexes, the stronger guest–guest interactions and potentially lower pore occupancy lead to a substantially smaller lattice expansion than that observed for pure [Emim][TFSI]-loaded ZIF-8.

To further confirm the interaction between $Li_{0.2}[Emim]_{0.8}[TFSI]$ and ZIF-8, infrared (IR) spectra were recorded for both pristine ZIF-8 and $Li_{0.2}[Emim]_{0.8}[TFSI]$@ZIF-8 samples at varying loading levels, as shown in Fig. 5(a). Several characteristic peaks were identified, providing insights into molecular interactions and structural integrity. For ZIF-8, the peak located at 1146 cm^{-1} related to C-N stretching vibration [29]. The band at 1583.8 cm^{-1} could be assigned as the C=N stretch mode [30,31]. The band at 995.1 cm^{-1} could be assigned as the C=C – N twisting mode (out-of-plane bending) [32]. The bands at 1310.9 cm^{-1} could be attributed to the stretching vibration of C-C in aromatic rings and the absorption peak at 1172 cm^{-1} were characterized by C-N stretching vibration [33]. The bands at 693.8 and 684.6 cm^{-1} related to the out-of-plane bending of organic ring. These peaks above in the ZIF-8 skeleton did not shift when the ZIF-8 was filled with $Li_{0.2}[Emim]_{0.8}[TFSI]$. However, as depicted in Fig. 4(b) and (c), the band at 420 cm^{-1}, which corresponded to the Zn-N stretching vibration within ZIF-8 [30], shifted to a lower wavenumber as the uptake of $Li_{0.2}[Emim]_{0.8}[TFSI]$ inside the ZIF-8 cages increases. Fig. 5(d) demonstrated that this shift exhibits a linear relationship with the occupied ratio of $Li_{0.2}[Emim]_{0.8}[TFSI]$ within the ZIF-8 cages.

For the $[Emim]^+$ cation, the band at 1166.7 cm^{-1} was attributed to N–C–H rocking vibrations [34,35], while the bands at 1346.6 cm^{-1} and 788.7 cm^{-1} corresponded to H–C–H rocking and wagging vibrations, respectively [35]. For $[TFSI]^-$, the band at 509.6 cm^{-1} was assigned to the C–S=O stretching vibration [36], and the band at 598.3 cm^{-1}

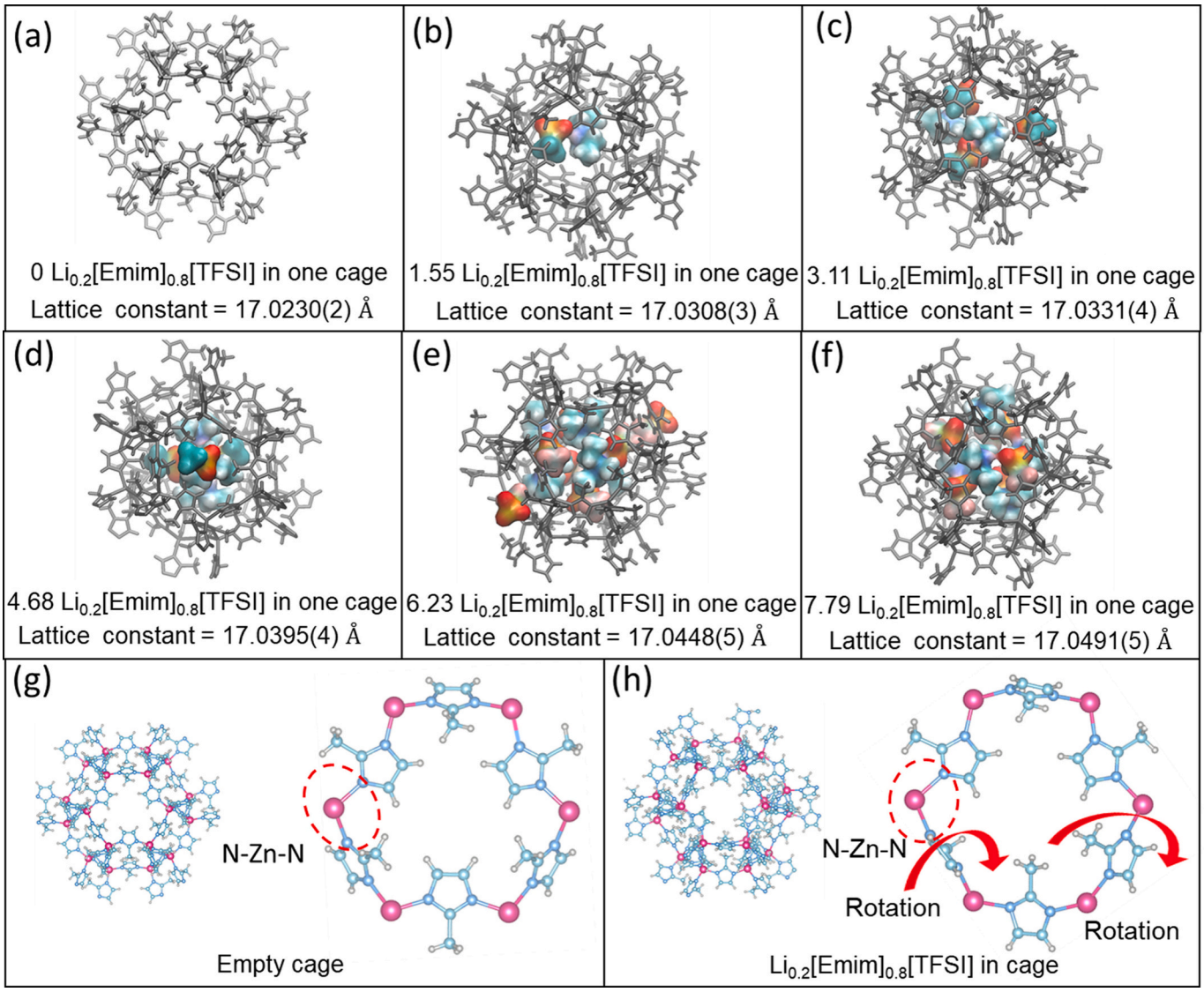

Fig. 4. Artwork of a ZIF-8 cage structure showing the effect of increasing $Li_{0.2}[Emim]_{0.8}[TFSI]$ loading: (a) pristine ZIF-8 cage and ZIF-8 cages containing an average of (b) 1.55, (c) 3.11, (d) 4.68, (e) 6.23, and (f) 7.79 $Li_{0.2}[Emim]_{0.8}[TFSI]$ ion pairs per cage (Constructed based on the experimental BET and XRD results.). Window structure of (g) ZIF-8 empty cages and (h) ZIF-8 cages combined with $Li_{0.2}[Emim]_{0.8}[TFSI]$.

corresponded to the S–N–S bending vibration [34]. Additionally, the band at 1227.0 cm^{-1} was associated with the symmetric stretching vibration of the C-F bond, while the band at 568.9 cm^{-1} represented the asymmetric C-F bending vibration [37]. Finally, the band at 739.6 cm^{-1} was attributed to the asymmetric S-N stretching vibration [35]. As shown in Fig. 5(b) and (e), the band at 1051.8 cm^{-1} was attributed to the O=S=O symmetric stretching vibration of $[TFSI]^-$[36]. The wavenumber of S=O stretching mode increased dramatically, once Li-IL goes inside in ZIF-8. The wavenumber of S=O stretching mode decrease, when the uptake of Li-IL increase in ZIF-8. Fig. 5(f) further confirmed a linear relationship between this peak shift and the occupied ratio of $Li_{0.2}[Emim]_{0.8}[TFSI]$ inside ZIF-8 cages.

The tetrahedral Zn-N bonds in ZIF-8 are inherently flexible, allowing their bond angles to adjust and enabling the framework to accommodate guest molecules by expanding. The introduction of $Li_{0.2}[Emim]_{0.8}[TFSI]$ ion pairs introduces charged species into the ZIF-8 framework, altering the local electrostatic environment and weakening the Zn-N coordination bonds, leading to structural expansion. Infrared (IR) spectroscopy results further support this observation, as the peak corresponding to the N–Zn–N stretching vibration shifts to a lower wavenumber, indicating a decrease in vibrational frequency and a weakening of the N–Zn–N bond as the cage structure expands, which also align with the theory of the "swing effect". Presumably, the rotation of the organic ligand, 2-methylimidazole, leads to a weakening of the N–Zn–N bonds, reducing their structural rigidity and contributing to the overall flexibility of the ZIF-8 framework. Because the Zn-N coordination bonds define the cage geometry, they are the most sensitive to structural expansion, leading to the pronounced spectral response upon cage deformation. Additionally, the bulky $[TFSI]^-$ anions interact with the imidazolium cations ($[Emim]^+$), exerting outward pressure on the framework. As more $Li_{0.2}[Emim]_{0.8}[TFSI]$ molecules enter the pores, steric hindrance (spatial crowding) further drives expansion by reducing repulsion between guest molecules. The ZIF-8 lattice constant increases progressively with higher loading, reaching a maximum expansion of +0.153% when the cages are fully occupied. Moreover, the peak associated with the O=S=O stretching vibration in the $[TFSI]^-$ anion also shifts to a lower wavenumber. This shift is attributed to the migration of $Li_{0.2}[Emim]_{0.8}[TFSI]$ ion pairs into the cages, which disrupts the interactions between the ion pairs and weakens the O=S=O bond strength.

The slight variation of the lattice constant (~0.15%) is associated with cage expansion induced by the Li-IL incorporation, because the lattice constant shows a linear relationship with the amount of Li-IL

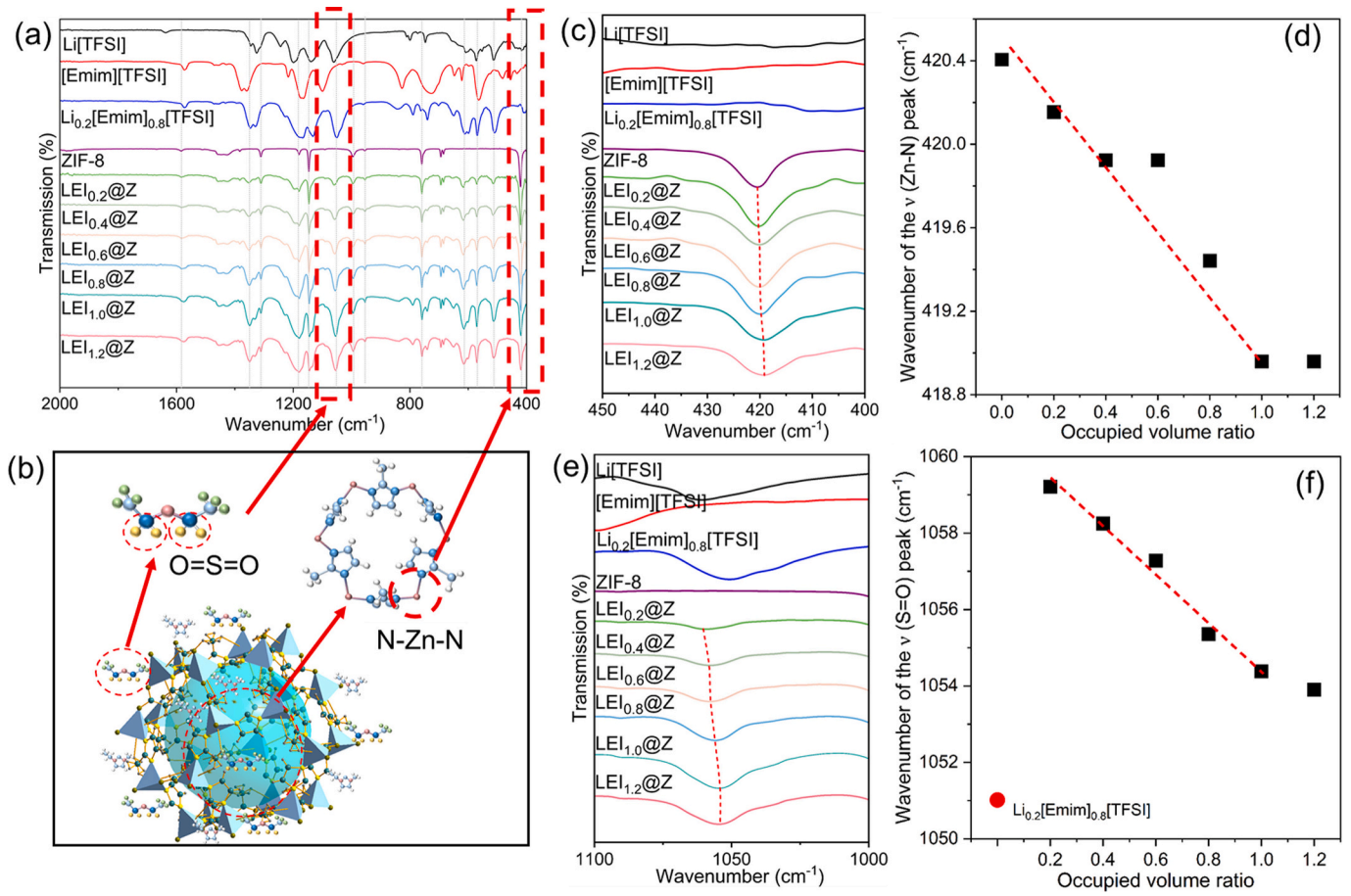

Fig. 5. (a) IR spectra of LEI@ZIF from 2000 cm^{-1} to 400 cm^{-1}, (b) LEI@ZIF structure related to IR spectrum, IR spectra of (c) $\nu_{(Zn\text{-}N)}$ and (e) $\nu_{(O=S=O)}$ from ZIF-8 skeleton, The peak position related to (d) $\nu_{(Zn\text{-}N)}$ and (f) $\nu_{(O=S=O)}$ in the function of occupied volume ratio of ZIF-8 cages.

combined with the ZIF-8 framework. The minor lattice expansion can be attributed to two possible factors. First, it is related to the "swing effect" of the ZIF-8 framework, as shown in Fig. 4 (h) and (g). The flexible Zn–mIm coordination network allows structural adjustment upon guest molecule confinement, resulting in slight cage expansion. Second, the expansion may also originate from the elongation/weakened coordination of the Zn-N bonds. The wavenumber of the Zn-N stretching vibration in the IR spectra also decreases linearly with increasing Li-IL content in Fig. 5(d). According to the harmonic oscillator model, a lower stretching vibration frequency indicates a decrease in the bond force constant, suggesting weakened Zn-N coordination and a tendency toward bond elongation. Therefore, the red shift of the Zn-N stretching vibration peak indicates that the Zn-N coordination environment becomes slightly weakened and more flexible after Li-IL incorporation, which is consistent with the observed lattice expansion of the ZIF-8 framework. These results suggest that both swing effect and slight Zn-N bond elongation contribute to the observed cage expansion.

The ionic conductivities were obtained from the impedance spectra of bulk [Emim][TFSI], bulk $Li_{0.2}[Emim]_{0.8}[TFSI]$, [Emim][TFSI]@ZIF-8, and $Li_{0.2}[Emim]_{0.8}[TFSI]$@ZIF-8 (Supplementary Information). As shown in Fig. 6(a), the maximum total conductivity of $EI_{1.2}$@ZIF-8 reaches 4.14(4) $mS{\cdot}cm^{-1}$ at 80 °C. This value is approximately two orders of magnitude lower than that of bulk [Emim][TFSI]. The corresponding activation energy for $EI_{1.0}$@ZIF-8 is 0.23(2) eV (Fig. 6(b)), reflecting only a ~ 6% increase in the energy barrier for ion. For the lithium-containing confined electrolyte, $LEI_{1.2}$@ZIF-8 exhibits a maximum total conductivity of 0.649(4) $mS{\cdot}cm^{-1}$ at 80 °C, which is approximately one order of magnitude lower than $EI_{1.2}$@ZIF-8 and about two orders of magnitude lower than bulk $Li_{0.2}[Emim]_{0.8}[TFSI]$ @ZIF-8, as shown in Fig. 6(c). The activation energy of $LEI_{1.0}$@ZIF-8 is 0.26(1) eV, corresponding to a ~ 14% increase in transport barrier compared to bulk $Li_{0.2}[Emim]_{0.8}[TFSI]$ (Fig. 6(d)). Notably, upon increasing the loading of $Li_{0.2}[Emim]_{0.8}[TFSI]$@ZIF-8 within the pores, the activation energy further decreases to 0.15(1) eV for $LEI_{1.2}$@ZIF-8, which is significantly lower than that of the bulk $Li_{0.2}[Emim]_{0.8}[TFSI]$ (0.2289(2) eV). However, when the pore occupancy of ZIF-8 decreased below 60%, the activation energy increased markedly. Specifically, the activation energy reached 0.54(1) eV at 60% occupancy, corresponding to a 135% increase relative to the bulk $Li_{0.2}[Emim]_{0.8}[TFSI]$, and further increased to 0.75(2) eV at 40% occupancy, representing a 228% increase.

The total conductivity of $Li_{0.2}[Emim]_{0.8}[TFSI]$ is lower than that of pure [Emim][TFSI], while its activation energy is comparatively higher. This can be attributed to the interactions between Li^+ and $TFSI^-$. Instead of existing as free ions, Li^+ tends to form ion clusters with $TFSI^-$, which affects ion mobility. The O=S=O groups in $TFSI^-$ serve as electron donors, coordinating with Li^+ to form a solvation shell that stabilizes the cation in the IL environment. These stronger $Li^+ - TFSI^-$ interactions hinder Li^+ mobility, leading to reduced ionic conductivity and increased activation energy due to the additional energy required to break these interactions and facilitate ion transport. When [Emim][TFSI] and $Li_{0.2}[Emim]_{0.8}[TFSI]$ are encapsulated within the pores of ZIF-8, their conductivity decreases further, while the activation energy increases due to the immobilization effect of the ZIF-8 framework. A distinct transition point is observed in the LiTFSI-loaded ZIF-8 samples. When the pore occupancy exceeds 60%, the activation energy remains comparable to that of the neat ionic liquid, indicating that lithium-ion transport is largely unaffected by confinement. In contrast, a sharp

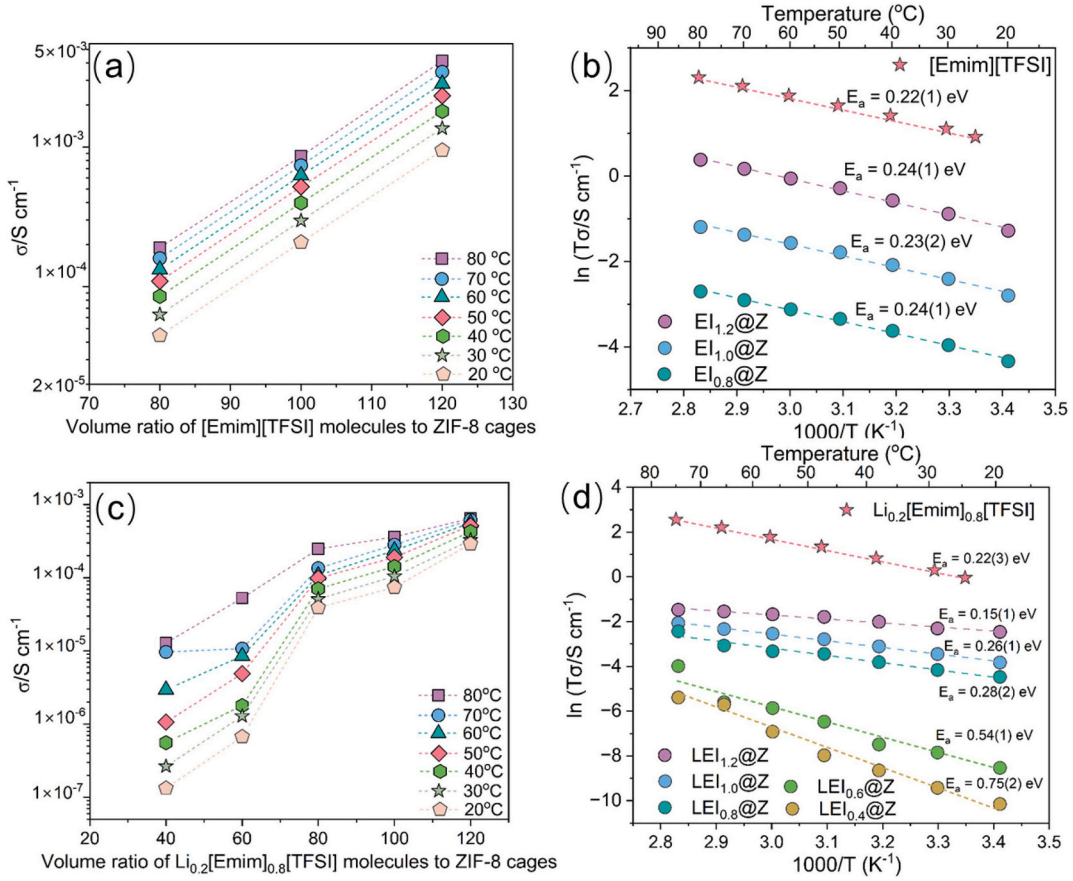

Fig. 6. (a) Total conductivity and (b) Activation energy of [Emim][TFSI] and [Emim][TFSI]@ZIF-8, (c) Total conductivity and (d) Activation energy of various concentrations of $Li_{0.2}[Emim]_{0.8}[TFSI]$ and $Li_{0.2}[Emim]_{0.8}[TFSI]$@ZIF-8 samples.

increase in activation energy occurs when the occupancy decreases below 60%. In Fig. 2, BET measurements revealed the emergence of a substantial fraction of empty cages in this low-occupancy regime, suggesting that the ZIF-8 pore network is no longer continuously filled. As a result, lithium-ion migration requires hopping across partially vacant regions, leading to a significant increase in the energy barrier for transport. Conversely, at occupancies above 80%, the intrinsic pore volume of ZIF-8 is essentially saturated, with excess ionic liquid residing in the voids between particles. The observation that the activation energy in this regime closely matches that of the bulk ionic liquid indicates that ion transport through these gap region between particle proceeds via a mechanism similar to that in the neat liquid phase.

The rigid porous structure of ZIF-8 restricts the mobility of ionic species, limiting their ability to move freely and conduct charge. The small pore apertures (~3.4 Å) and strong host–guest interactions hinder ion diffusion, particularly for Li^+, which forms stronger interactions with $TFSI^-$ in the confined space. Additionally, the disruption of continuous ion pathways within the ZIF-8 framework forces ions to navigate through restricted channels, further reducing conductivity. Moreover, the activation energy for ion transport increases because ions must overcome stronger electrostatic and steric hindrances imposed by the ZIF-8 structure. In this confined environment, ion hopping becomes less efficient, requiring more energy to facilitate conduction. Numerous studies have also revealed the confinement effect of ZIF-8 on various guest molecules, demonstrating its ability to regulate molecular mobility and interactions within its porous framework. Schmidt et al. conducted an in-depth thermodynamic and kinetic analysis to investigate ethane diffusion in ZIF-8 [38]. Their findings revealed that ethane diffusion is a hindered process, governed by a transition state in which an ethane molecule must pass through the aperture (gate) between adjacent ZIF-8 cages, which are formed by methylimidazole linkers. This transition state significantly influences the diffusion dynamics of ethane within the framework. Similarly, Tang employed MD simulations to study the diffusion behavior of water in ZIF-8 [21]. The results demonstrated that the self-diffusion coefficient of confined water within the ZIF-8 cages is generally one to two orders of magnitude lower than that of bulk water. This reduction is attributed to the restricted pore size and strong confinement effects imposed by the ZIF-8 framework, which limit the mobility of water molecules. Kanj et al. explored the conduction properties of an IL, specifically 1-butyl-3-methylimidazolium bis(trifluoromethylsulfonyl)amide ([Bmim][TFSA]) within the regular pores of the relatively rigid and crystalline HKUST-1 metal-organic framework. The findings revealed that under high loadings, both anions and cations are compelled to occupy the same pore windows simultaneously. Due to the restricted pore size of the MOF, preventing the simultaneous passage of both ions, the opposing drift directions of the ions result in mutual blockage and a transient jamming of the pore windows [39].

Bhattacharyya et al. and Pfaffenhuber et al. introduced liquid non-aqueous salt solutions into solid insulating particles to synthesize a new type of lithium electrolyte, known as the “soggy sand” electrolyte [40,41]. They observed that conductivity was significantly enhanced, exhibiting a percolation-type behavior characteristic of interfacial conductivity. Riess et al. introduced water and ZrO_2, and found the conductivity enhancement in the liquid-solid composite to be attributable to an adsorption of the anion by the oxide, and hence break up of the ion pair, leading to an enhanced Li + concentration in the boundary surrounding the oxides, so called space charge layer [42]. Building on this concept, we deduce that when the amount of $Li_{0.2}[Emim]_{0.8}[TFSI]$ is increased to 120% occupied volume ratio, exceeding the maximum capacity of the ZIF-8 cages, a portion of the IL accumulates at the particle

interfaces. This interfacial localization lowers the activation energy, as ions can diffuse along the particle boundaries rather than overcoming the higher energy barriers associated with hopping through the ZIF-8 cage windows.

Lithium transference numbers were determined in $Li_{0.2}$[Emim]$_{0.8}$[TFSI] liquid electrolyte and $LEI_{1.2}$@ZIF pellet electrolyte. The lithium transference number of the $Li_{0.2}$[Emim]$_{0.8}$[TFSI] liquids exhibited a relatively low lithium-ion transference number of 0.11, as shown in Fig. 7(a). This behavior can be attributed to the strong coordination between Li^+ and $TFSI^-$ anions, which leads to ion pairing or aggregation and limits the mobility of free lithium ions. The lithium transference number of the $LEI_{1.2}$@ZIF pellet further decreased to 0.04, as shown in Fig. 7(b), indicating that lithium ions contribute minimally to the overall ionic conductivity. Previous studies have reported that the incorporation of ZIF-8 can enhance the lithium-ion transference number through its well-defined microporous structure and confinement effect [11,12]. The interconnected cages and narrow pore apertures of ZIF-8 can selectively restrict the migration of bulky anionic species while facilitating Li^+ transport through the pore network, thereby promoting preferential lithium-ion conduction. However, this behavior was not observed in the present system. Instead, the addition of ZIF-8 resulted in a lower t_{Li+}. One possible explanation is that lithium-ion transport predominantly occurs along grain boundaries and interparticle interfaces rather than through the internal ZIF-8 pore network. In this case, the confinement effect of the ZIF-8 cages is not fully utilized, and the expected enhancement in lithium-ion selectivity cannot be achieved. Furthermore, the relatively poor mechanical integrity of the ZIF-8 pellet may lead to inadequate interparticle contact and increased interfacial resistance. As shown in Fig. 7(c), the $LEI_{1.2}$@ZIF pellet exhibits a significantly higher interfacial impedance, which can hinder efficient Li^+ transport and contribute to the observed decrease in lithium-ion transference number.

The electrochemical stability window of the composite electrolytes was evaluated by linear sweep voltammetry (*LSV*), and the corresponding curves are presented in Fig. 7(d). The $LEI_{1.2}$@ZIF pellet exhibits a wide electrochemical stability window of approximately 5.4 V **(vs. Li/Li$^+$)**, indicating excellent oxidative stability. Such a broad stability window enables compatibility with most commercially available lithium-ion battery cathode materials, including $LiCoO_2$, $LiNi_xMn_yCo_zO_2$ (NMC), $LiNi_{0.8}Co_{0.1}Mn_{0.1}O_2$, $LiNi_{0.5}Mn_{1.5}O_4$ (LNMO), and $LiFePO_4$.

The $Li_{0.2}$[Emim]$_{0.8}$[TFSI] liquid electrolyte and $LEI_{1.2}$@ZIF pellet electrolyte were assembled into $LiCoO_2$||Li coin cells. Fig. 7(e) shows the rate performance of cells at room temperature. The coin cell assembled with $Li_{0.2}$[Emim]$_{0.8}$[TFSI] liquid electrolyte delivered average discharge capacities of 115(1), 113(1), 111(2), 108(1), and 100(2) mAh g^{-1} at 0.2, 0.4, 0.6, 1, and 2C, respectively. The coin cell assembled with $LEI_{1.2}$@ZIF pellet delivered average discharge capacities of 108(4), 66 (3), 88(1), 45(1), and 1.9(2) mAh g^{-1} at 0.2, 0.4, 0.6, 1, and 2C, respectively. As shown in Fig. 7(f), The $LEI_{1.2}$@ZIF pellet has a capacity retention of 74.9% after 100 cycles at 0.2C at room temperature. Compared with the pure lithium-salt-containing ionic liquid, $Li_{0.2}$[Emim]$_{0.8}$[TFSI], the quasi-solid-state electrolyte $LEI_{1.2}$@ZIF, prepared by incorporating the lithium-salt-containing ionic liquid into the ZIF-8 framework, exhibits inferior electrochemical performance in lithium batteries. This behavior can be attributed to several factors. First, as shown in Fig. 6(c), the ionic conductivity of $LEI_{1.2}$@ZIF is approximately two orders of magnitude lower than that of the pristine $Li_{0.2}$[Emim]$_{0.8}$[TFSI], indicating a substantial reduction in ion transport kinetics after confinement within the ZIF-8 framework. Second, the batteries employing $LEI_{1.2}$@ZIF exhibit a significantly higher interfacial resistance than those using the pure ionic liquid electrolyte, as evidenced by the electrochemical impedance spectra in Fig. 7(c). The increased interfacial impedance suggests less efficient charge transfer and poorer electrode/electrolyte interfacial contact, which further limits the overall electrochemical performance.

This study demonstrates that incorporating lithium-salt-containing ionic liquids into MOF frameworks is a strategy for the development of solid-state or quasi-solid-state lithium-ion electrolytes. Nevertheless, several challenges remain. Although confinement of the ionic liquid within the MOF framework successfully produces a solid-state electrolyte, it also leads to a reduction in ionic conductivity and an increase in activation energy for ion transport. To overcome these limitations,

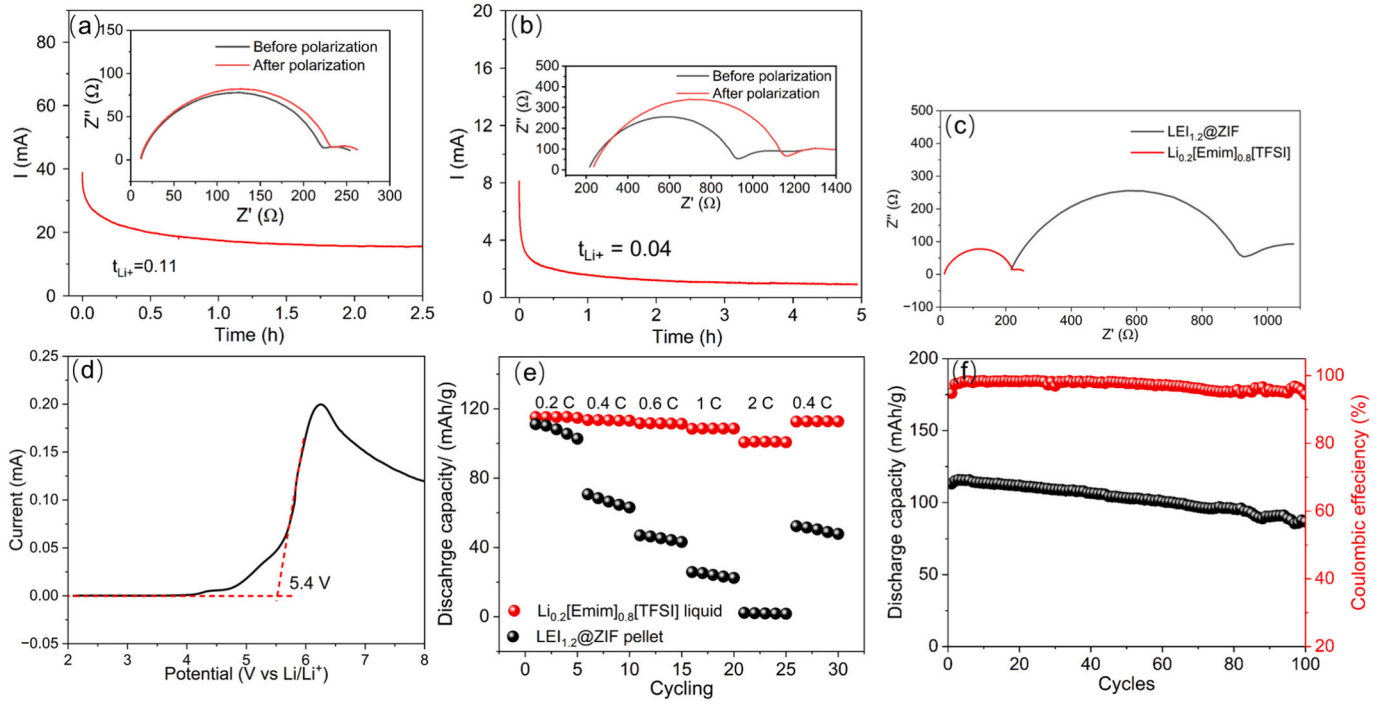

Fig. 7. DC polarization curve and the EIS before and after polarization for Li symmetric cells with (a) $Li_{0.2}$[Emim]$_{0.8}$[TFSI] and (b) $LEI_{1.2}$@ZIF pellet. (c) EIS for Li symmetric cells with $Li_{0.2}$[Emim]$_{0.8}$[TFSI] liquid and $LEI_{1.2}$@ZIF pellet. (d) LSV curves of $LEI_{1.2}$@ZIF pellet. (e) Rate performances of the $LiCoO_2$||$LEI_{1.2}$@ZIF||Li cell and $LiCoO_2$|| $Li_{0.2}$[Emim]$_{0.8}$[TFSI]||Li cell at different current density. (f) Long-term cycle performance of the $LiCoO_2$||$LEI_{1.2}$@ZIF||Li coin cell at 0.2C.

future work should explore MOFs with larger pore cavities and wider apertures, which may facilitate lithium-ion migration between neighbouring cages and thereby reduce the activation energy associated with ion transport. Furthermore, pellets fabricated solely from MOF particles often exhibit poor mechanical integrity, and their relatively rough surfaces can increase interfacial resistance, adversely affecting electrochemical performance. To address these issues, the incorporation of suitable polymer binders during electrolyte fabrication may improve mechanical robustness, enhance pellet densification, and produce smoother electrode–electrolyte interfaces, ultimately reducing interfacial impedance and improving battery performance.

4. Conclusion

A lithium-ion-containing IL, $Li_{0.2}[Emim]_{0.8}[TFSI]$, was successfully encapsulated within the pores of ZIF-8, leading to a systematic and continuous expansion of its sodalite cages. This structural expansion is associated with a weakening of the N–Zn–N coordination environment upon guest incorporation, indicating a clear host–guest interaction between the ionic liquid and the MOF framework. In parallel, the confined $Li_{0.2}[Emim]_{0.8}[TFSI]$ perturbs the local ion-pairing environment, disrupting cation–anion interactions and thereby reducing the effective O=S=O bond strength within the $[TFSI]^-$ anion. The optimized composite, $LEI_{1.2}$@ZIF-8, achieves a maximum ionic conductivity of 0.649 (4) $mS{\cdot}cm^{-1}$ at 80 °C under anhydrous conditions. Despite this enhancement relative to the empty framework, the conductivity of $Li_{0.2}[Emim]_{0.8}[TFSI]$ within ZIF-8 remains approximately one order of magnitude lower than that of the neat ionic liquid, and the corresponding activation energy is comparatively high, reflecting the constraining effect of the rigid ZIF-8 pore network on Li^+ transport. These results underscore a fundamental trade-off between structural confinement and ion mobility: while the MOF scaffold provides a mechanically robust, shape-persistent host and suppresses liquid flow or leakage, it simultaneously imposes energetic barriers to long-range ion migration. The lithium transference number of $LEI_{1.2}$@ZIF-8 pellet is 0.04 and the electrochemical window is 5.4 *V*. The $LiCoO_2$||Li coin cells with $LEI_{1.2}$@ZIF pellet has a capacity retention of 74.9% after 100 cycles at 0.2C at room temperature. Overall, this study demonstrates the promise of Li-IL@MOF hybrid composites as quasi-solid-state or solid-state Li-ion conductors and provides important structure–property insights that can guide the rational design of next-generation electrolytes for advanced lithium-ion battery technologies.

CRediT authorship contribution statement

Wen Yang: Writing – original draft, Methodology, Investigation, Formal analysis, Conceptualization. **Christian Rodenbücher:** Writing – review & editing, Supervision. **Jiangshui Luo:** Writing – review & editing, Supervision. **Carsten Korte:** Writing – review & editing, Supervision.

Author statement

Wen Yang: Materials synthesis, Characterization, Investigation, Data analysis, Writing.

Christian Rodenbücher: Supervision, Review & editing.

Jiangshui Luo: Supervision, Review & editing.

Carsten Korte: Supervision, Review & editing.

Declaration of competing interest

The authors declare that they have no known competing financial interests or personal relationships that could have appeared to influence the work reported in this paper.

Acknowledgements

We would like to appreciate China Scholarship Council (CSC No. 202206240005) for the International Cooperative Training Project for Innovative Talents (project No.: CXXM2011280411). We gratefully acknowledge K. Klafki and A. Everwand for technical support. J. Luo acknowledges National Natural Science Foundation of China (project No.: 22378270 and 21776120), Sichuan Science and Technology Program (project No.: 2023JDRC0013), Hohhot Science and Technology Program (project No.: 2023-JieBangGuaShuai-Gao-3) and Natural Science Foundation of Fujian Province, China (project No.: 2023J01254). Open Access publication funded by the Deutsche Forschungsgemeinschaft (DFG, German Research Foundation)—Grant No. 491111487.

Appendix A. Supplementary data

Supplementary data to this article can be found online at https://doi.org/10.1016/j.ssi.2026.117268.

Data availability

All relevant data are presented in the main text and in the electronic Supporting Information (ESI).

References

[1] C. Sun, J. Liu, Y. Gong, D.P. Wilkinson, J. Zhang, Nano Energy 33 (2017) 363.
[2] Z. Gao, H. Sun, L. Fu, F. Ye, Y. Zhang, W. Luo, Y. Huang, Adv. Mater. 30 (17) (2018) e1705702.
[3] Q. Zhao, X. Liu, S. Stalin, K. Khan, L.A. Archer, Nat. Energy 4 (5) (2019) 365.
[4] X. Cheng, J. Pan, Y. Zhao, M. Liao, H. Peng, Adv. Energy Mater. 8 (7) (2017).
[5] Q. Zhao, S. Stalin, C.-Z. Zhao, L.A. Archer, Nat. Rev. Mater. 5 (3) (2020) 229.
[6] J.C. Bachman, S. Muy, A. Grimaud, H.H. Chang, N. Pour, S.F. Lux, O. Paschos, F. Maglia, S. Lupart, P. Lamp, L. Giordano, Y. Shao-Horn, Chem. Rev. 116 (1) (2016) 140.
[7] C. Wang, K. Fu, S.P. Kammampata, D.W. McOwen, A.J. Samson, L. Zhang, G. T. Hitz, A.M. Nolan, E.D. Wachsman, Y. Mo, V. Thangadurai, L. Hu, Chem. Rev. 120 (10) (2020) 4257.
[8] P. Dong, X. Zhang, W. Hiscox, J. Liu, J. Zamora, X. Li, M. Su, Q. Zhang, X. Guo, J. McCloy, M.K. Song, Adv. Mater. 35 (32) (2023) e2211841.
[9] Z. Wu, Y. Yi, F. Hai, X. Tian, S. Zheng, J. Guo, W. Tang, W. Hua, M. Li, ACS Appl. Mater. Interfaces 15 (18) (2023) 22065.
[10] L. Wang, Y. Han, X. Feng, J. Zhou, P. Qi, B. Wang, Coord. Chem. Rev. 307 (2016) 361.
[11] S. Li, B. Chen, Z. Shi, Q. Tong, J. Weng, J. Energy Storage 102 (2024).
[12] F. Tao, L. Tian, Z. Liu, R. Cui, M. Liu, X. Kang, Z. Liu, J. Mater. Chem. A 10 (26) (2022) 14020.
[13] M. Salado, R. Fernández de Luis, T.H. Smith, M. Hasanpoor, S. Lanceros-Mendez, M. Forsyth, Batteries Supercaps 7 (9) (2024).
[14] M. Sun, J. Li, H. Yuan, X. Zeng, J. Lan, Y. Yu, X. Yang, Mater. Today Energy 29 (2022).
[15] Z. Wang, R. Tan, H. Wang, L. Yang, J. Hu, H. Chen, F. Pan, Adv. Mater. 30 (2) (2018).
[16] O. Shekhah, R. Swaidan, Y. Belmabkhout, M. du Plessis, T. Jacobs, L.J. Barbour, I. Pinnau, M. Eddaoudi, Chem. Commun. (Camb.) 50 (17) (2014) 2089.
[17] K. Fujie, R. Ikeda, K. Otsubo, T. Yamada, H. Kitagawa, Chem. Mater. 27 (21) (2015) 7355.
[18] J. Hessling, L. Dick, S. Keil, V. Alizadeh, M.R. Hansen, B. Kirchner, M. Schonhoff, J. Phys. Chem. B 129 (25) (2025) 6372.
[19] J.V. Morabito, L.Y. Chou, Z. Li, C.M. Manna, C.A. Petroff, R.J. Kyada, J. M. Palomba, J.A. Byers, C.K. Tsung, J. Am. Chem. Soc. 136 (36) (2014) 12540.
[20] W. Zheng, Z. Li, Y. Dai, X. Li, X. Ruan, X. Jiang, X. Zhang, G. He, Chem. Eng. Sci. 280 (2023).
[21] Y.B. Tang, S.J. Xie, Phys. Chem. Chem. Phys. 24 (8) (2022) 5220.
[22] T. Yu, Q. Cai, G. Lian, Y. Bai, X. Zhang, X. Zhang, L. Liu, S. Zhang, Chem. Eng. J. 419 (2021).
[23] S.A. Moggach, T.D. Bennett, A.K. Cheetham, Angew. Chem. Int. Ed. Eng. 48 (38) (2009) 7087.
[24] S. Bansal, N. Kaur, G.R. Chaudhary, S.K. Mehta, A.S. Ahluwalia, J. Chem. Eng. Data 59 (12) (2014) 3988.
[25] N. Doebelin, R. Kleeberg, J. Appl. Crystallogr. 48 (Pt 5) (2015) 1573.
[26] P. Hofmann, J.W. Wells, J. Phys. Condens. Matter 21 (1) (2009) 013003.
[27] W. Yang, C. Rodenbücher, J. Luo, C. Korte, J. Mater. Sci. 61 (15) (2026) 10421.
[28] B. Chang, Y. Yang, H. Jansen, F. Ding, K. Mølhave, H. Sun, Adv. Mater. Interfaces 5 (9) (2018).
[29] M. Shahmirzaee, A. Hemmati-Sarapardeh, M.M. Husein, M. Schaffie, M. Ranjbar, Microporous Mesoporous Mater. 307 (2020).

[30] J. Liu, J. He, L. Wang, R. Li, P. Chen, X. Rao, L. Deng, L. Rong, J. Lei, Sci. Rep. 6 (2016) 23667.
[31] M. He, J. Yao, Q. Liu, K. Wang, F. Chen, H. Wang, Microporous Mesoporous Mater. 184 (2014) 55.
[32] P. Cheng, Y.H. Hu, J. Phys. Chem. C 118 (38) (2014) 21866.
[33] C.-S. Wu, Z.-H. Xiong, C. Li, J.-M. Zhang, RSC Adv. 5 (100) (2015) 82127.
[34] P.J. Chengula, T. Pogrebnaya, A. Pogrebnoi, J. Mol. Liq. 299 (2020).
[35] N.R. Dhumal, K. Noack, J. Kiefer, H.J. Kim, J. Phys. Chem. A 118 (13) (2014) 2547.
[36] Y. Li, M. Zhang, X. Wang, Z. Li, L. Zhao, Electrochim. Acta 222 (2016) 1308.
[37] R. Rathika, O. Padmaraj, S.A. Suthanthiraraj, Ionics 24 (1) (2017) 243.
[38] B.E. Schmidt, P. Cnudde, V. Van Speybroeck, L. Vanduyfhuys, J. Phys. Chem. C 128 (43) (2024) 18509.
[39] A.B. Kanj, R. Verma, M. Liu, J. Helfferich, W. Wenzel, L. Heinke, Nano Lett. 19 (3) (2019) 2114.
[40] A.J. Bhattacharyya, J. Maier, Adv. Mater. 16 (9–10) (2004) 811.
[41] C. Pfaffenhuber, M. Gobel, J. Popovic, J. Maier, Phys. Chem. Chem. Phys. 15 (42) (2013) 18318.
[42] S. Raz, K. Sasaki, J. Maier, I. Riess, Solid State Ionics 143 (2001) 181.